vehicles

MDPI

Article

Research on the Dynamic Response Characteristics of a Railway Vehicle Under Curved Braking Conditions

Chunguang Zhao [1], Zhiyong Fan [2], Peixuan Li [2], Micheale Yihdego Gebreyohanes [2], Zhiwei Wang [2] and Jiliang Mo [2,*]

[1] Tieke Zongheng (Tianjin) Technology Development Co., Ltd., Tianjin 301700, China
[2] State Key Laboratory of Rail Transit Vehicle System, Southwest Jiaotong University, Chengdu 610031, China
* Correspondence: jlmo@swjtu.cn

Abstract: When a railway train runs along a curved track with braking, the dynamic behaviors of the vehicle are extremely complex and difficult to accurately reveal due to the coupling effects between the wheel–rail interactions and the disc–pad frictions. Therefore, a rigid–flexible coupled trailer car dynamics model of a railway train is established. In this model, the brake systems and vehicle system are dynamically coupled via the frictions within the braking interface, wheel–rail relationships and suspension systems. Furthermore, the effectiveness of the established model is validated by a comparison with the field test data. Based on this, the dynamic response characteristics of vehicle under curve and straight braking conditions are analyzed and compared, and the influence of the curve geometric parameters on vehicle vibration and operation safety is explored. The results show that braking on a curve track directly affects the vibration characteristics of the vehicle and reduces its operation safety. When the vehicle is braking on a curve track, the lateral vibration of the bogie frame significantly increases compared to the vehicle braking on a straight track, and the vibration intensifies as the curve radius decreases. When the curved track maintains equilibrium superelevation, the differences in primary suspension force, wheel–rail vertical force, and wheel axle lateral force between the inner and outer sides of the first and second wheelsets are relatively minor under both straight and curved braking conditions. Additionally, under these circumstances, the derailment coefficient is minimized. However, when the curve radius is 7000 m, with a superelevation of 40 mm, the maximum dynamic wheel load reduction rate of the inner wheel of the second wheelset is 0.54, which reaches 90% of the allowable limit value of 0.6 for the safety index, and impacts the vehicle running safety. Therefore, it is necessary to focus on the operation safety of railway trains when braking on curved tracks.

Keywords: curve braking; dynamic characteristics; brake system; rigid–flexible coupled dynamics; railway train

check for updates

Received: 10 January 2025
Revised: 7 February 2025
Accepted: 12 February 2025
Published: 15 February 2025

Citation: Zhao, C.; Fan, Z.; Li, P.; Gebreyohanes, M.Y.; Wang, Z.; Mo, J. Research on the Dynamic Response Characteristics of a Railway Vehicle Under Curved Braking Conditions. *Vehicles* **2025**, *7*, 18. https://doi.org/10.3390/vehicles7010018

1. Introduction

When a railway train traverses curved tracks at high velocities, the dynamic response of the vehicle system becomes significantly more complex compared to its behavior on straight tracks [1]. If the geometric parameters of the curved track are mismatched with the vehicle speed, the centrifugal force during curve negotiation will not be fully balanced, posing a threat to the safe operation of the vehicle [2]. Furthermore, during emergency braking, the strong friction between the brake disc and the brake pad intensifies the wheel–rail interactions, suspension forces, and vehicle vibration responses, making them more pronounced and difficult to predict [3,4]. Due to the harsh operating conditions and complex work scenarios of a railway train, especially a high-speed train, emergency braking on curved tracks poses a significant challenge to train running safety at high-speed ranges [5]. Therefore, a comprehensive understanding of the vehicle system's dynamic response characteristics under curved braking conditions is essential for ensuring the safe operation of such trains.

There are many studies on the dynamic behavior of railway vehicles, yet they often overlook the coupling effects between the braking system and the vehicle systems, as well as the dynamic response of the vehicle during braking [6–8]. Zhai et al. [9] developed a vehicle–track spatial coupling dynamic model and analyzed the wheel–rail lateral dynamic interaction performance indicators when the train traverses a curve with a small radius. Hiroyuki et al. [10] developed a nonlinear elastic model of leaf springs for the simulation of multibody vehicle systems by considering the nonlinear dynamic coupling effect between finite rotations and deformation of leaf springs and modeling the distributed inertia and stiffness of leaf springs. SUÁREZ et al. [11] analyzed the operational safety of vehicles passing through highly elastic curved tracks in the presence of broken rails, based on multibody dynamics and finite element methods. Weilguny et al. [12] explored the interaction between the wheel and the rail when the vehicle passed through a curved track based on the established vehicle–track coupling dynamics model. The research found that the wheel–rail forces had a significant impact on the track and the rail profile when the vehicle passed through the curved track. Generally, research in this field has primarily concentrated on aspects like curve passability, vehicle dynamic behavior, and wheel–rail interactions. However, studies evaluating the dynamic response characteristics of railway vehicles under complex curved track conditions are still relatively scarce. Additionally, although existing research has primarily focused on vehicle dynamics, the analysis considering the brake system is relatively less emphasized.

Fortunately, researchers globally have extensively studied the dynamic characteristics of high-speed train braking systems through both simulation and experimental methods [13,14]. Currently, the primary focus of brake system research centers on interface contact behavior [15–17], frictional heat [18–20], and frictional wear [21–23]. Sinou et al. [24] studied the dynamic characteristics and noise properties of TGV using finite element simulation and bench testing. Xiang et al. [25] studied the effects of the shape and installation orientation of the brake block on the friction at the braking interface and the dynamic behavior. Wang et al. [26] studied the effect of different friction block hole diameters on the stick–slip vibration at the disc–block interface in the brake system. They found that friction blocks with specific hole diameters could effectively suppress the stick–slip vibration phenomenon at the disc–block interface, improving the braking stability of the trailer bogie. Zhang et al. [27] investigated the impact of wheel polygonal wear on the temperature and vibration of the high-speed train brake system. It was found that wheel polygonal wear would lead to intensified fluctuations in the contact area between the disc and the block of the brake system, enhanced vibrations, and increased interface temperatures. Wang [28] studied the temperature and vibration characteristics of the brake system under the action of thermo-mechanical coupling. They also conducted a comparative analysis with the results obtained when the thermo-mechanical coupling was neglected and reached the conclusion that the self-excited vibration of the braking system was significantly enhanced under the thermo-mechanical coupling state. The above research is of great significance for understanding the contact friction at the disc–block interface of the braking system and for its optimization and regulation. The aforementioned studies provide methods for investigating the dynamic response of brake systems. However, these studies are solely focused on the brake system itself and overlook the interaction with the entire vehicle system.

Overall, the research on the dynamic interactions between vehicle systems and brake systems is quite limited. Some studies focus primarily on vehicle dynamics, while others delve into braking dynamics; however, comprehensive investigations that integrate both aspects are rare. Moreover, there is a notable lack of information on the dynamic response of vehicles under curved braking conditions [29]. Additionally, during actual operations of high-speed trains, the brake and vehicle systems influence each other. This interaction may become more pronounced as trains navigate through complex curved tracks and require braking for speed adjustments or stopping.

To address this issue, the paper develops a rigid-flexible coupled dynamics model for a high-speed train's trailer car that incorporates the braking systems, based on vehicle dynamics and finite element theory. The model is validated through experimental data. Subsequently, a comparative study examines the vehicle vibrations, suspension responses, wheel–rail interactions, and other characteristics under both curved- and straight-track braking conditions. Additionally, the research systematically investigates the influence of the geometric parameters of the curved track on vehicle vibration and safety during curved-track braking. This work is expected to provide theoretical support for enhancing the operational performance and safety of the vehicle system under such conditions.

2. Rigid–Flexible Coupling Dynamics Model of High-Speed Train Trailer

2.1. Dynamics Model of Trailer Car

Based on the structural characteristics and operating principles of a certain type of high-speed train trailer car in China, a dynamics model of the trailer car including disc brake systems was established, as shown in Figure 1. The vehicle system mainly consists of one car body, two bogies, four wheelsets and eight axle boxes. In addition, three sets of foundation braking devices are installed on the wheelset axles of the trailer bogie. In the foundation braking unit, the brake disc is fixedly connected to the wheelset axle, and the brake caliper is suspended from the bogie frame. The movements between the various components of the vehicle are simulated by spring-damping units. The main dynamic parameters of the high-speed train trailer system are shown in Table 1.

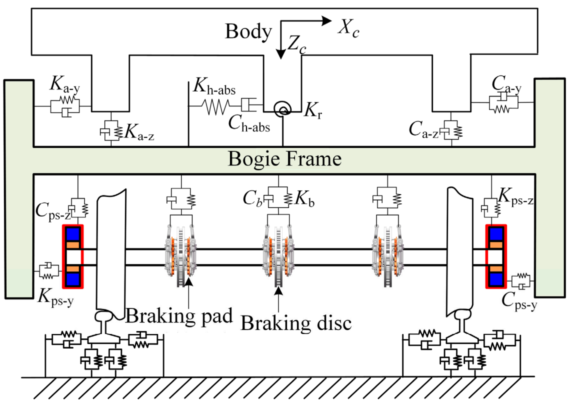

Figure 1. Schematic diagram of trailer car dynamics model.

In order to accurately obtain the dynamic response of the vehicle system during friction braking between the brake disc and the pad, detailed modeling of the trailer bogie is carried out considering the mutual friction between the brake disc and the pad as well as the flexible deformation of the components of the brake system, as shown in Figure 2. During the braking process, by applying the braking force F to the brake caliper, the caliper rotates around its axis, causing the brake pad to come into contact with the brake disc and generate a friction force in the opposite direction to the rotation of the wheelset. Then, the friction force is transmitted to the wheel–rail interface through the wheelset axle to form a longitudinal creep force that hinders the forward movement of the wheelset, thus realizing the braking of the vehicle.

Table 1. Main dynamic parameters of high-speed train trailer car.

Parameters	Value
Track gauge (mm)	1435
Fixed wheelbase of the bogie (mm)	2500
Distance between backs of wheel flanges (mm)	1353
Lateral displacement of the wheel rolling circle (mm)	1493
Length between bogie centers (mm)	17,375
Frame moment of inertia $x/y/z$ (kg·m^2)	1236/1233/2336
Primary suspension supporting stiffness $x/y/z$ (kN/m)	920/920/886
Secondary suspension supporting stiffness $x/y/z$ (kN/m)	133/133/203
Brake disc spacing (mm)	420
Brake disc mass (kg)	119.1
Brake disc moment of inertia $x/y/z$ (kg·m^2)	3.3/3.3/6.4
Brake caliper mass (kg)	14.7
Brake caliper moment of inertia $x/y/z$ (kg·m^2)	0.14/0.26/0.12
Hanger mass (kg)	10.5
Hanger moment of inertia $x/y/z$ (kg·m^2)	0.24/0.18/0.08
Carbody mass (t)	38.9
Carbody moment of inertia x/y/z (t·m^2)	126/1905/1798
Brake friction coefficient	0.35
Wheel–rail friction coefficient	0.4

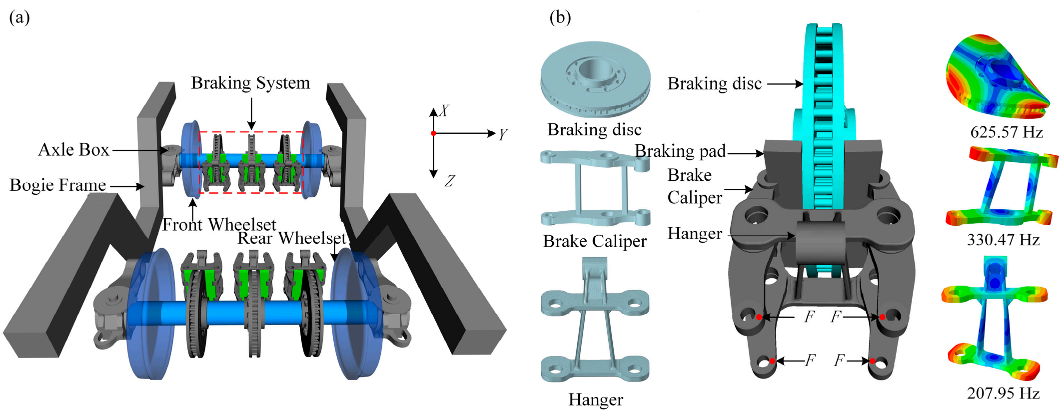

Figure 2. Dynamics model of: (**a**) bogie; and (**b**) brake system.

In this model, the modal superposition method and the finite element method are adopted to achieve the flexible modeling of the brake disc, the brake caliper and the hanger. During the process of flexible dynamics modeling, the elastic deformation of structures such as the brake caliper and the brake disc is solved by means of the modal superposition method. However, the large number of degrees of freedom in the finite element model of the brake system limits the computation and solution of the dynamic response. For this reason, the substructure analysis method is adopted to reduce the degrees of freedom of the model and couple it into the vehicle dynamics model, thus realizing the establishment of the vehicle dynamics model considering the flexible brake systems. The dynamics model of the flexible brake systems is shown in Figure 2b. The relevant parameters of the brake system's components are listed in Tables 2 and 3. Figure 3 shows the specific modeling process of the rigid–flexible coupled trailer dynamics model including the flexible brake systems.

Table 2. Finite element model parameters of brake components.

Component	Element Type	Number Elements	Degrees of Freedom of Master Node	Minimum Element Size (mm)
Brake caliper	Hexahedron	266,280	356	0.9
Brake disc	Hexahedron	385,566	326	1.1
Hanger	Tetrahedron	164,654	325	1.1

Table 3. Material parameters of brake components.

Component	Material	Elastic Modulus (MPa)	Young's Modulus	Density (kg/m^3)
Brake caliper	cast iron	169 000	0.28	7 800
Brake disc	65Mn	206 000	0.3	7 850
Hanger	cast iron	169 000	0.28	7 800

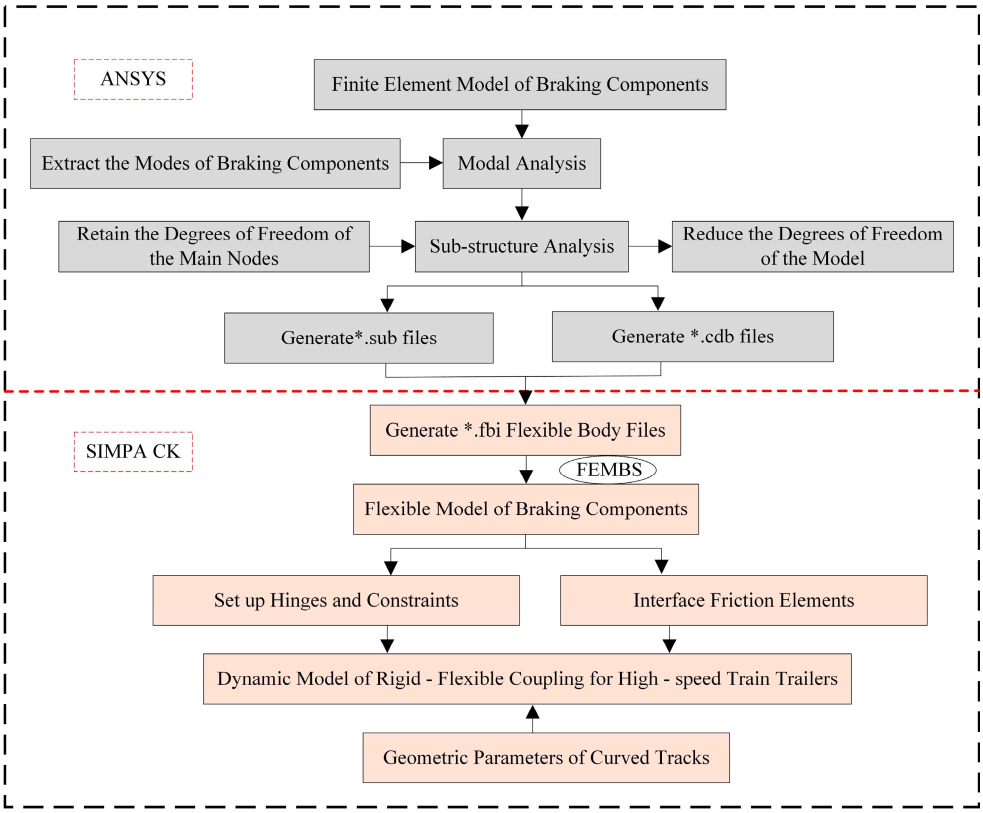

Figure 3. Flowchart of rigid–flexible coupled dynamics model of trailer car.

The model effectively facilitates the study of the dynamic response characteristics of vehicle key components during braking on curved tracks with varying radii. However, due to limitations in modeling techniques and computational efficiency, the model was simplified reasonably throughout its development. Some factors, such as damping elements, flexible deformations of components, and friction effects, were omitted. These simplifications are not expected to significantly affect the analysis outcomes. Moreover, this allows the model to run efficiently on a high-performance workstation, completing simulations and analyses within ten minutes when utilizing eight threads.

Based on the multibody dynamics theory, considering the interactions between various vehicle components, including the articulation, primary and secondary suspension systems, and taking into account nonlinear characteristics such as lateral bump stops, vertical dampers, and yaw dampers, the governing differential equations of the high-speed train's trailer car in the rigid–flexible coupled dynamics model can be expressed as [9,27]:

$$\begin{cases} \boldsymbol{M}\ddot{\boldsymbol{q}} + \boldsymbol{D}\dot{\boldsymbol{q}} + \boldsymbol{K}\boldsymbol{q} + \boldsymbol{C}_{\mathrm{q}}^{\mathrm{T}}\boldsymbol{\lambda} = \boldsymbol{Q}_{\mathrm{e}} + \boldsymbol{Q}_{\mathrm{v}} + \boldsymbol{Q}_{\mathrm{wr}} \\ \boldsymbol{C}(\boldsymbol{q},t) = \boldsymbol{0} \end{cases} \tag{1}$$

In the equation, $\boldsymbol{M}$ is the mass matrix of the system; $\boldsymbol{D}$ is the damping matrix; K is the stiffness matrix; $\boldsymbol{q}$ is the generalized coordinate vector of the system; $\mathbf{C}_{\mathrm{q}}^{\mathrm{T}}$ is the transpose of the system Jacobian matrix; λ is the Lagrange multiplier; and $\boldsymbol{Q}_{\mathrm{e}}$ is the generalized external force vector. $\boldsymbol{Q}_{\mathrm{v}}$ is the generalized inertial force vector; $\boldsymbol{Q}_{\mathrm{wr}}$ is the generalized vector of wheel–rail forces; and $\boldsymbol{C}(\boldsymbol{q},t)$ represents the system constraint equations

2.2. Geometric Parameters of Curved Tracks

For the curve braking condition, a track model is developed based on the actual geometric parameters of the curved track. The force state of the wheelset when the trailer car passes through the curved track is shown in Figure 4. When the vehicle passes through a curved track, a large centrifugal acceleration a_L is generated, which intensifies the dynamic interaction between the outer wheel and rail. Therefore, the surface of the outer track rail is raised by h relative to that of the inner track, and this is called the superelevation value of the curve track. In this way, the centripetal acceleration a_X provided by the vehicle's gravitational acceleration can balance the centrifugal acceleration generated when the vehicle passes through the curved section, thereby improving the vehicle's curve passing performance.

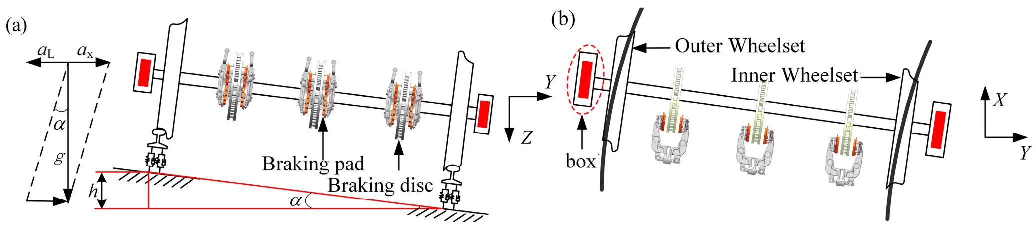

Figure 4. Force diagram of wheelset when passing through curved track: (**a**) front view and (**b**) top view.

The equilibrium superelevation value for a vehicle passing through a curve can be calculated using the following equation [30]:

$$h = \frac{11.8v^2}{r} \tag{2}$$

In the equation, r is the radius of the curve, and v is the speed of the vehicle while passing through the curve.

In the simulation analysis, the typical curve track conditions of the Beijing–Shanghai High-Speed Railway are selected. The curve track consists of a straight-line transition, curve–circular curve–transition, curve–straight line. Five typical curve radius parameters are selected, including 7000, 8000, 11,000, 12,000, and 14,000 m. The superelevation values are selected within the range of 40 to 220 mm. The specific geometric parameters of the curved track in the model are shown in Table 4.

Table 4. Geometric parameters of curved track.

Radius of the Circular Curve (m)	Straight-Line Length (m)	Transition Curve Length (m)	Circular Curve Length (m)	Actual Superelevation (mm)	Equilibrium Superelevation (mm)
7000	200	900	500	40~220	206
8000				40~220	180
11,000				40~220	131
12,000				40~220	120
14,000				40~220	103

When the train passes through the curved track section at high speed, according to the requirements of riding comfort, the length of the transition curve should meet [31]:

$$L \geq \frac{v_{\max}}{3.6} \frac{h}{[f]} \tag{3}$$

In the equation, h is the actual superelevation value; $v_{\max}$ is the maximum speed of the train while passing through the curve; and $[f]$ is the superelevation change rate. Under normal conditions, the superelevation change rate is 25.25 mm/s, while under difficult conditions, it is 30.86 mm/s. In the simulation analysis, the maximum superelevation value is set to 220 mm, and the train's speed while passing through the curve is 350 km/h. It is calculated that, under normal conditions, the length of the transition curve should be greater than 847.1 m. Therefore, the transition curve length of 900 m in the model satisfies the requirements.

The derailment coefficient is an important indicator for evaluating the running safety of railway vehicles, which can be calculated by:

$$\lambda = \frac{Q}{P} \tag{4}$$

In the equation, λ is the derailment coefficient, Q is the wheel weight; P is the lateral wheel–rail force.

The wheel load reduction rate is one of the key indicators for evaluating the running safety of railway vehicles, used to describe the variation in wheel–rail force distribution, which can be calculated by:

$$R = \frac{\Delta P}{P_{Max}} \tag{5}$$

In the equation, R is the wheel load reduction rate; ΔP is the wheel load difference; P_{Max} is the maximum vertical wheel–rail force between the two wheels of the wheelset.

2.3. Brake Disc–Pad Friction Model

The interaction between the brake disc and pad is crucial for simulating the braking behavior of trains. A detailed description of the high-speed train rigid–flexible coupled trailer car dynamics model is presented in Section 2.1. In this section, the brake disc–pad interaction model will be explained. This paper primarily focuses on the dynamic response characteristics of vehicles during high-speed emergency braking. Therefore, the stick–slip motion between the brake disc and brake pad is not considered. Instead, a friction model that accounts for the sliding friction between the brake disc and pad is established, as shown in Figure 5. The interface friction force between the brake disc and pad can be expressed as [32]:

$$F_f = \mu_s F_N \tag{6}$$

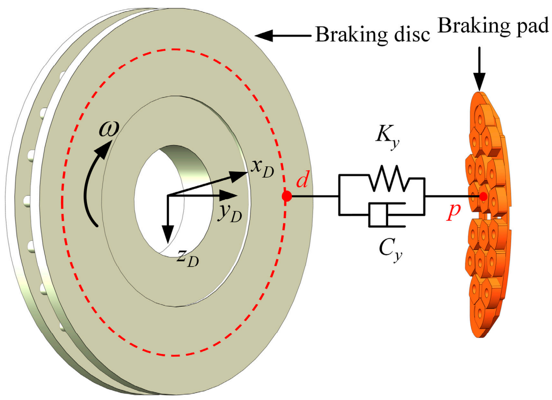

Figure 5. Diagram of brake disc–pad interaction.

In the equation, μ_s represents the sliding friction coefficient, and F_N denotes the normal force at the braking interface, which can be calculated as [29]:

$$F_N = \begin{cases} K_y r_{dpy} + C_y v_{\mathrm{dpy}}, v_{\mathrm{dpy}} > 0 \\ 0, v_{\mathrm{dpy}} < 0 \end{cases} \tag{7}$$

In the equation, K_y and C_y represent the contact stiffness and damping coefficient between the brake disc and pad, respectively; r_{dpy} and v_{dpy} represent the lateral relative displacement and velocity between the position d on the brake disc and the position p on the pad, respectively.

In the simulation process, the vehicle speed is kept constant to simulate complex braking conditions such as high-speed emergency braking and slope braking. The typical braking force of the brake system for high-speed trains ranges from 0 to 10 kN [32]. A braking force F is applied to one side of the brake caliper, as shown in Figure 2b.

To simulate the dynamic response of the vehicle system when passing through a circular curve with specific track geometry parameters under braking conditions, the braking force applied to the vehicle in the curve braking scenario is shown in Figure 6a. When investigating the dynamic response of the vehicle system under different braking forces, the braking force is adjusted during the vehicle's passage through the circular curve, while the braking force under straight-line braking conditions remains constant. Figure 6b shows the braking interface friction force of the brake system. It can be seen that due to the symmetric installation of the first and second wheelsets in the brake system, the direction of the interface friction force between the brake pads and the brake disc is opposite for the first and second wheelsets.

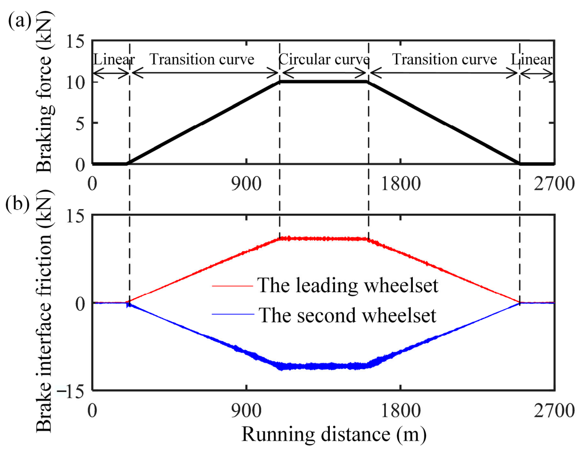

Figure 6. Curved braking conditions: (**a**) braking force; (**b**) interface friction force.

2.4. Wheel–Rail Interaction

The wheel–rail interaction is key to accurately calculating the wheel–rail forces and analyzing the dynamic behavior of the vehicle system. The wheel–rail normal force is primarily calculated using the nonlinear Hertzian elastic contact theory [33]:

$$P(t) = \begin{cases} \left[\frac{1}{G}\delta Z(t)\right]^{3/2} & , \quad \delta Z(t) > 0 \\ 0 & , \quad \delta Z(t) < 0 \end{cases} \tag{8}$$

In the equation, G is a constant determined by the wheel–rail geometric parameters and $\delta Z(t)$ is the elastic compression deformation at the normal contact point between the wheel and rail.

Using Kalker's linear creep theory, the longitudinal creep force F_x between the wheel and rail can be calculated as follows [9]:

$$F_x = -G_{\text{wr}}(ab)C_{11}\xi_x \tag{9}$$

The lateral creep force F_y between the wheel and rail can be calculated as follows [9]:

$$F_y = -G(ab)C_{22}\xi_y - G(ab)^{3/2}C_{23}\xi_\phi \tag{10}$$

Since Kalker's linear creep theory is only applicable to small creep rates and small spin conditions, to simulate cases with arbitrary creep rates and smaller spin values, the modified longitudinal and lateral creep forces can be obtained using the Shen–Hedrick–Elkins model as follows:

$$\begin{cases} F_x' = \frac{F'}{\sqrt{F_x^2+F_y^2}} \cdot F_x \\ F_y' = \frac{F'}{\sqrt{F_x^2+F_y^2}} \cdot F_y \end{cases} \tag{11}$$

In the equation, F_x' and F_y' represent the modified longitudinal and lateral creep forces, respectively. Meanwhile, F' is defined as [30,31]:

$$F' = \begin{cases} fN\left[\frac{\sqrt{F_x^2+F_y^2}}{fN} - \frac{1}{3}\left(\frac{\sqrt{F_x^2+F_y^2}}{fN}\right) + \frac{1}{27}\left(\frac{\sqrt{F_x^2+F_y^2}}{fN}\right)^3\right] & \left(\sqrt{F_x^2+F_y^2} \leqslant 3fN\right) \\ fN & \left(\sqrt{F_x^2+F_y^2} > 3fN\right) \end{cases} \tag{12}$$

In the equation, f represents the wheel–rail friction coefficient, and N is the normal force at the contact point.

3. Model Validation

To validate the established rigid–flexible coupled dynamics model of a high-speed train's trailer car, experimental field test data were used. During these tests, the vehicle operated at a speed of 300 km/h, and vertical vibration acceleration data from the bogie frame and axle box were collected at a sampling frequency of 5000 Hz. The placement of the acceleration sensors was consistent with those used in previous studies [34]. At the same time, a simulation analysis under identical operating conditions is conducted for the established dynamics model. The time–domain and frequency–domain results of the field test and simulation data are shown in Figures 7 and 8, respectively.

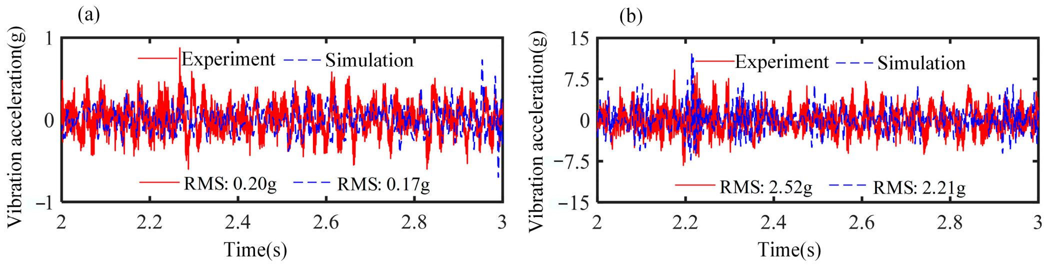

Figure 7. Comparison of experimental and simulation results in time domain of: (**a**) bogie frame; and (**b**) axle box.

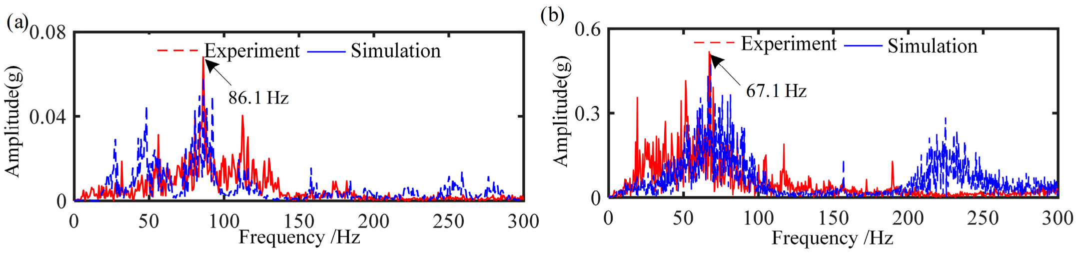

Figure 8. Comparison of experimental and simulation results in frequency domain of: (**a**) bogie frame; and (**b**) axle box.

Figure 7 shows that the root mean square (RMS) values of the bogie frame vibration acceleration from the field test and simulation analysis are 0.20 g and 0.17 g, respectively, while the RMS values of the axle box vibration acceleration are 2.52 g and 2.21 g, respectively. The simulation data are slightly smaller than the field test data, which is attributed to the neglect of the flexible deformation of the rails or wheelsets in the model. Additionally, the simulated track irregularities in the simulation differ from the actual operating conditions. Figure 8 shows that the bogie frame spectrum exhibits a frequency of 86.1 Hz, which corresponds to a harmonic of the wheel rotational frequency, while the 67.1 Hz peak in the axle box spectrum is induced by track irregularity excitation.

The differences between the simulation results and experimental results in the frequency range below 50 Hz may be due to the neglect of the flexible deformation of components such as the bogie and axle box in the coupled dynamics model. Overall, the field experimental data for the bogie frame and axle box are in close agreement with the simulation results. Therefore, the established trailer car dynamics model effectively captures the primary vibration characteristics of the vehicle system, thereby validating the model's effectiveness.

4. Analysis and Discussion

4.1. Comparison of Vehicle System Dynamic Response Under Curved and Straight-Line Braking Conditions

To study the difference in the dynamic response of the vehicle system under curved braking and straight-line braking conditions, a comparative analysis is first conducted. The analysis examines the lateral vibration response of the bogie frame under braking conditions at a speed of 350 km/h. This includes scenarios on a circular curved track with a radius of 8000 m and a cant deficiency of 40 mm, as well as during braking on a straight track. The results are shown in Figure 9. It was found that the standard deviation (STD) of the lateral vibration acceleration of the bogie frame during curved braking is 1.66 m·s^{-2}, which is a 52.3% increase compared to the result of 1.09 m·s^{-2} during straight-line braking. conmtuibution 9b shows the frequency spectrum of the lateral vibration acceleration of the bogie frame, which includes the wheelset rotational frequency 33.6 Hz and its harmonics.

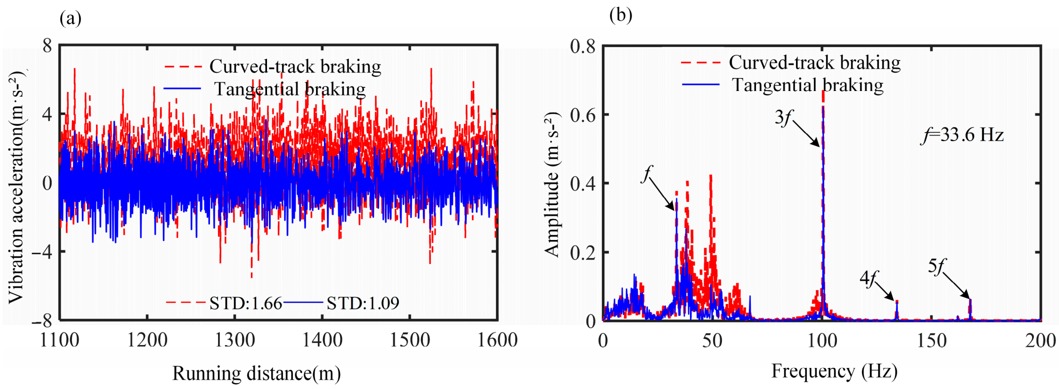

Figure 9. Lateral vibration acceleration of bogie frame in: (**a**) time and (**b**) frequency domain.

Lateral vibration directly impacts wheel–rail interaction, which is closely related to safety indicators such as the derailment coefficient and lateral wheel–rail force. Vertical vibration affects the stability of wheel–rail contact, the distribution of wheel loads, and the wear of wheel–rail interfaces, consequently influencing vehicle stability and ride comfort. Since this article primarily focuses on the safety of vehicles during curved braking, it mainly analyzes lateral and vertical vibrations.

Further statistical analysis is conducted to evaluate the standard deviations of the lateral and vertical vibration accelerations of the bogie frame during braking on circular curves with a radius of 8000 m and varying superelevation values, as well as on straight tracks, as depicted in Figure 10. In the figure, equilibrium superelevation refers to the height by which the outer rail is raised relative to the inner rail on a curved track when a train operates at its equilibrium speed. This ensures that the train achieves balanced operation solely through gravity, without relying on the lateral forces between the wheel and rail, such as centrifugal force or track lateral force. Deficient superelevation and excess superelevation refer to the height of the outer rail being lower and higher, respectively, than the equilibrium superelevation relative to the inner rail.

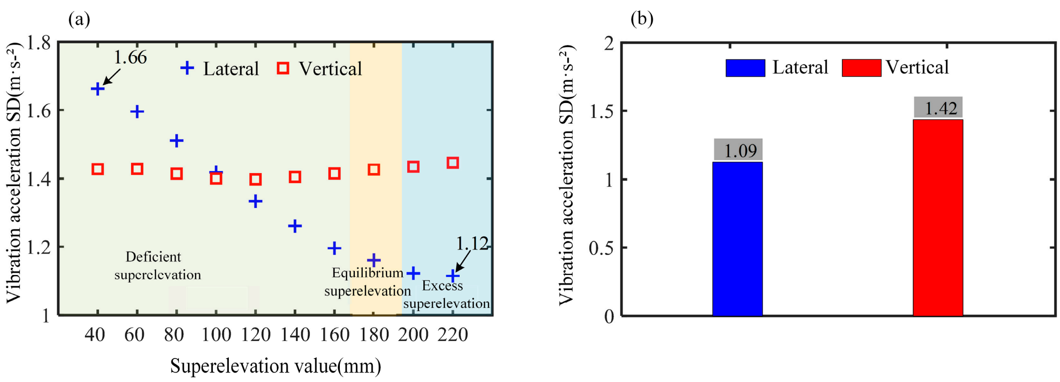

Figure 10. Standard deviation of frame vibration acceleration: (**a**) curved; and (**b**) straight-line braking.

It can be observed that the standard deviation of the lateral vibration acceleration of the bogie frame under curved track braking conditions is consistently higher than that experienced during straight-line braking. Furthermore, the intensity of the lateral vibrations increases as the superelevation decreases. Specifically, when the superelevation is 40 mm, the standard deviation of the lateral vibration acceleration of the bogie frame is 1.66 m·s^{-2}, which is 48.2% higher compared to the result with a superelevation of 220 mm. Additionally, the difference in vertical vibration of the bogie frame between curved and straight-line braking conditions is relatively minor, suggesting that vertical vibrations are primarily driven by track irregularities rather than the geometric parameters of the curved track.

The primary vertical suspension forces on both the inner and outer sides of the first and second wheelsets, as well as the wheel–rail vertical and axle lateral forces under both curved and straight-line braking conditions, are crucial for understanding the dynamic response and ensuring the safety of the vehicle being studied. Figure 11 presents the calculated results of the primary vertical suspension forces on the inner and outer sides of the first and second wheelsets during braking on circular track curves with a radius of 8000 m and different superelevation values, as well as on straight track.

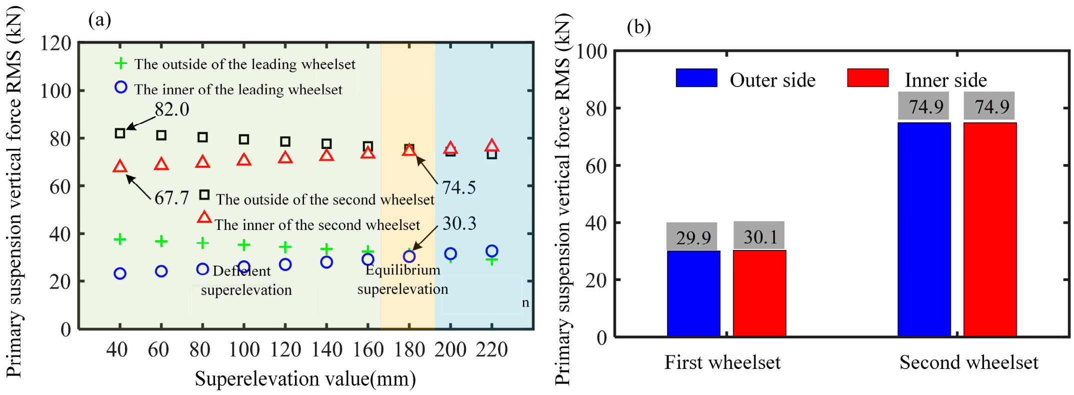

Figure 11. Primary vertical suspension force: (**a**) curved; and (**b**) straight-line braking.

It can be observed that under braking conditions, the primary vertical suspension force on the first wheelset is smaller than that on the second wheelset. This is due to the symmetric installation of the first and second wheelset brake systems, with the brake calipers, hangers, and other braking components suspended from the bogie frame via brake suspension joints. During braking, the bogie frame experiences an upward interface friction force (-Z direction) from the first wheelset's brake system and a downward interface friction force (Z direction) from the second wheelset's brake system. This results in the bogie frame undergoing pitch motion, which in turn causes a significant difference in the primary vertical suspension force of the first and second wheelsets under braking conditions.

In addition, during braking on a curved track with equilibrium superelevation, the root mean square (RMS) values of the vertical forces for the first and second wheelsets on the inner and outer sides are 30.3 kN and 74.5 kN, respectively, which show little difference compared to the vertical forces under straight-line braking conditions. When the superelevation is less than 180 mm, the vehicle is in an inadequate superelevation condition, and the primary vertical suspension forces on the outer sides of the first and second wheelsets are greater than those on the inner sides. Specifically, when the superelevation is 40 mm, the primary vertical suspension forces on the outer and inner sides of the second wheelset are 82.0 kN and 67.7 kN, respectively, which represent increases of 10.1% and decreases of 9.1% compared to the results under equilibrium superelevation. In contrast, when the superelevation exceeds 180 mm, the vehicle is in an excessive superelevation condition, and the vertical suspension force on the inner side is greater than that on the outer side. Therefore, the mismatch between the curve radius and the superelevation has a significant impact on the primary vertical suspension force responses on both the inner and outer sides of the vehicle system.

Figure 12 shows the RMS values of the wheel–rail vertical forces on the inner and outer wheels of the first and second wheelsets when the vehicle is braking on circular tracks with a curve radius of 8000 m and different superelevation values, as well as on straight tracks.

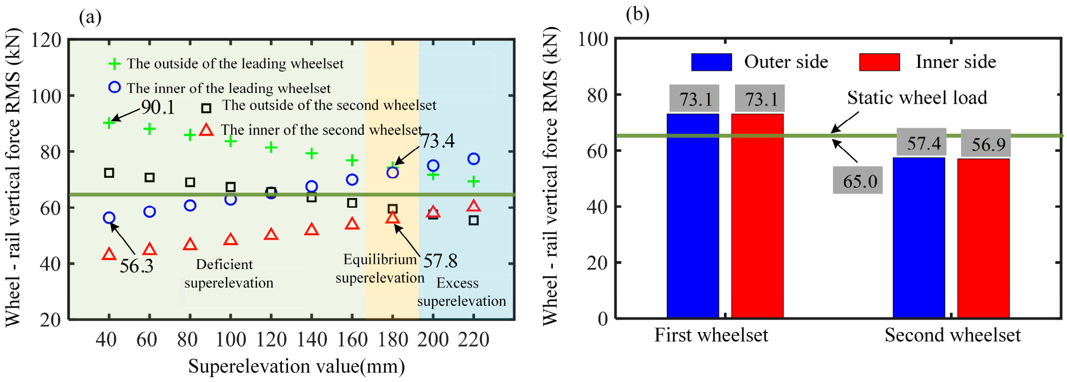

Figure 12. Vertical wheel–rail force: (**a**) curved; and (**b**) straight-line braking.

The results indicate that, during both curve and straight-line braking, the vertical wheel–rail forces on the inner and outer wheels of the first wheelset are greater than those on the inner and outer wheels of the second wheelset. This is due to the fact that the first wheelset's axle experiences interface frictional forces directed downward (in the Z-direction) from the brake systems, while the second wheelset's axle experiences interface frictional forces directed upward (in the -Z direction) from the brake systems.

Furthermore, during curved braking, when the track superelevation is equal to the equilibrium superelevation, the RMS values of the vertical wheel–rail forces on the inner and outer wheels of the first and second wheelsets are 72.4 kN and 57.8 kN, respectively. These values are 7.4 kN and 7.2 kN higher than the static wheel load, which is similar to the results observed under straight-track braking conditions. However, when the superelevation is less than 180 mm, the vertical wheel–rail force on the outer wheel becomes greater than that on the inner wheel. Specifically, when the superelevation is 40 mm, the vertical wheel–rail force on the left wheel of the first wheelset reaches 90.1 kN, which is a 22.7% increase compared to the result under equilibrium superelevation. When the superelevation exceeds 180 mm, the vertical wheel–rail force on the inner wheel becomes greater than that on the outer wheel.

Figure 13 shows the lateral forces on the axles of the first and second wheelsets of the vehicle during braking on a circular curve with a radius of 8000 m and different superelevation values, compared to braking on a straight track.

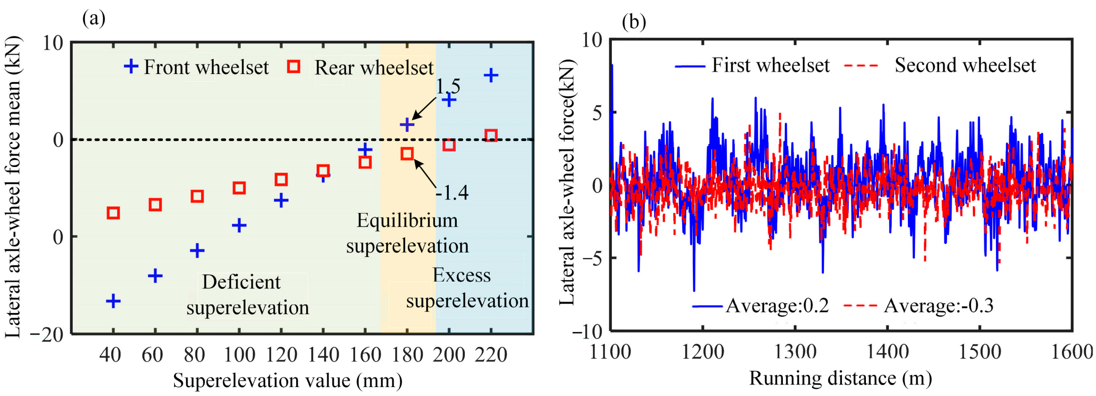

Figure 13. Lateral axle-wheel force: (**a**) curved braking; (**b**) straight-line braking.

It can be observed that during curved braking, compared to the second wheelset, the superelevation has a greater impact on the lateral force on the axle of the first wheelset. When the superelevation is less than 140 mm, both the first and second wheelsets experience lateral axle forces in the direction of the outer track (in the -Y direction), with the lateral force on the first wheelset being larger than that on the second. This is due to the larger vertical wheel–rail force on the first wheelset and the greater centrifugal force acting on it. When the superelevation is at the equilibrium value, the difference in the average lateral wheelset axle force of the first and second wheelsets during curved braking and straight-line braking is relatively small. When the superelevation exceeds 180 mm, the first wheelset carries a lateral wheelset axle force in the direction of the inner track (in the Y direction). During straight-line braking, the average lateral axle forces on both the first and second wheelsets are relatively small. Therefore, during curve braking, particularly when the vehicle is operating with a large superelevation deficit, the larger lateral axle-wheel force on the first wheelset could exacerbate wheel–rail wear and worsen the vehicle's operational environment.

4.2. The Impact of Geometric Parameters of Curved Track on the Dynamic Response of Vehicle Systems

In the curve braking operation of the vehicle, the geometric parameters of the curved track have a significant impact on the running state and vibration characteristics of the bogie frame. Figure 14 shows the roll angle of the frame when the vehicle operates under braking conditions on curved tracks with five different radii and superelevation values of 40 mm and 220 mm, respectively. Bogie frame roll angle refers to the roll angle of the bogie frame around its longitudinal axis (travel direction). The results indicate that the roll angle of the bogie frame decreases as the curve radius decreases. This is because, with a smaller curve radius, the centrifugal force generated by the vehicle while passing through the circular curve track increases, which in turn reduces the roll angle of the frame.

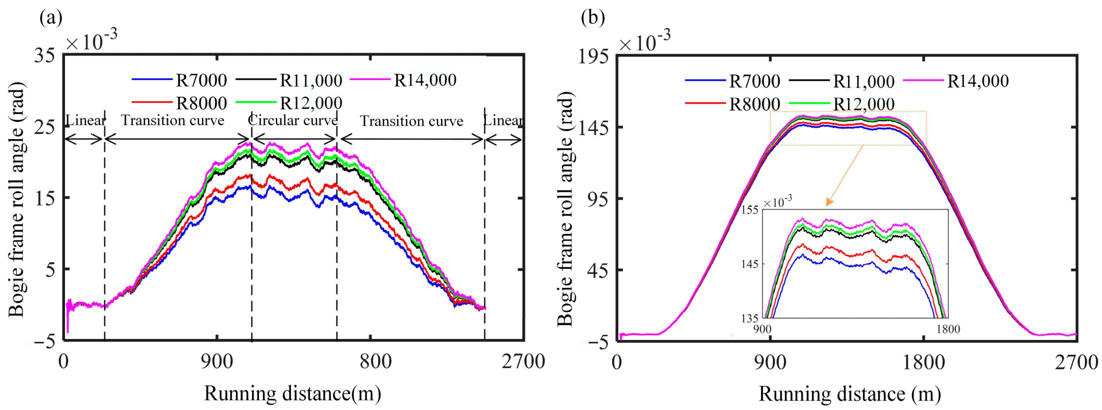

Figure 14. Frame roll angle with the superelevation of: (**a**) 40; and (**b**) 220 mm.

The statistical analysis of the lateral and vertical vibration acceleration standard deviations of the bogie frame during braking on circular tracks with different curve radii is shown in Figure 15. Figure 15a indicates that the smaller the superelevation value, the greater the impact of the curve radius on the lateral vibration acceleration standard deviation of the bogie frame. Specifically, when the superelevation is 40 mm and the curve radius is 7000 m, the lateral vibration acceleration standard deviation of the frame is 1.74 m/s^2, which is 4.8%, 22.5%, 27.9%, and 39.2% higher compared to the results for curve radii of 8000 m, 11,000 m, 12,000 m, and 14,000 m, respectively. Conversely, when the track superelevation is larger, the impact of the curve radius on the lateral vibration acceleration standard deviation is reduced. Figure 15b shows that the curve radius, superelevation, and other track geometry parameters have a smaller effect on the vertical vibration acceleration standard deviation of the bogie frame. Therefore, in the actual service of the vehicle, special attention should be paid to the operational safety of the vehicle under braking conditions with smaller curve radii.

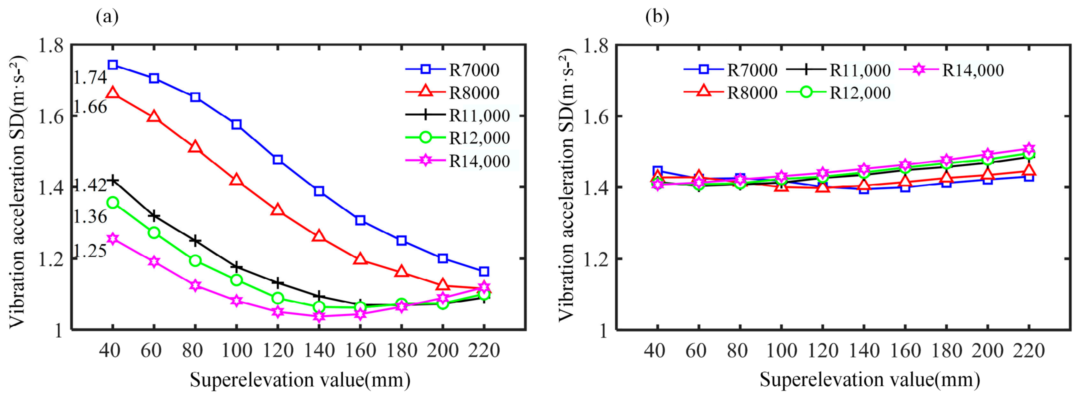

Figure 15. Standard deviation of bogie frame vibration acceleration: (**a**) lateral; and (**b**) vertical vibration acceleration.

The derailment coefficient and wheel load reduction rate during braking on curves with different geometric parameters are of significant importance for evaluating the operational safety of vehicles. Figure 16a illustrates the calculated derailment coefficient for the left wheel of a wheelset during curve braking, highlighting how superelevation significantly influences the lateral force on the wheelset axle across various curve radii, specifically for tracks with a superelevation of 40 mm. The results indicate that the derailment coefficient increases as the curve radius decreases. Specifically, when the curve radius is 7000 m, the maximum derailment coefficient is 0.21, which is 90.9% higher compared to the result for a radius of 14,000 m. This is because, with smaller curve radii, the inadequate superelevation increases, and the increase in lateral wheel–rail force on the outer wheel is greater than the increase in vertical wheel–rail force.

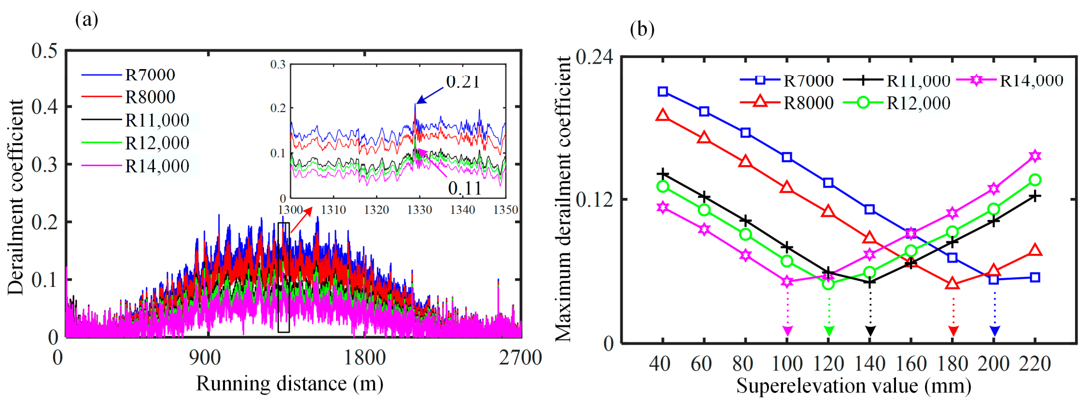

Figure 16. Derailment coefficient: (**a**) time domain results; (**b**) statistical results.

Figure 16b shows the maximum derailment coefficient of the outer wheel of a wheelset during braking on circular tracks with different curve radii and superelevation values. The results indicate that as the curve superelevation increases, the maximum derailment coefficient first decreases and then increases, with a minimum value occurring at the equilibrium superelevation. Therefore, setting the track superelevation to the balanced value can reduce the derailment coefficient, thereby enhancing the operational safety during the curved braking of vehicles.

When the vertical wheel–rail force falls below the static wheel load and the reduction in wheel load is excessive, it can easily lead to vehicle derailment, thereby compromising the vehicle's operational safety. As can be seen from Figure 12, when the vehicle brakes, the vertical wheel–rail force of the second wheelset is lower than the static wheel load. Therefore, the maximum dynamic wheel load reduction rates of the inner and outer wheels of the second wheelset during the vehicle's curved braking are further compared and analyzed, as shown in Figure 17.

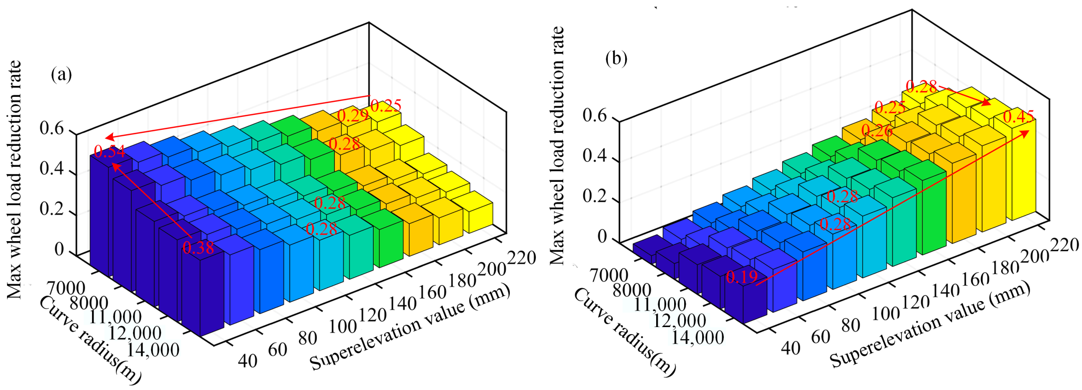

Figure 17. Maximum wheel load reduction rate: (**a**) inner; and (**b**) outer wheel of second wheelset.

Figure 17a shows that the maximum wheel load reduction rate of the inner wheel of the second wheelset continuously increases as the curve radius and the superelevation value decrease. Specifically, when the curve radius is 7000 m and the superelevation value is 40 mm, the maximum dynamic wheel load reduction rate of the inner wheel of the second wheelset is 0.54. This is because the vehicle is in an inadequate superelevation state, and the centrifugal force when passing through the curve is greater than the centripetal force provided by gravity, which in turn leads to a relatively large dynamic load reduction of the inner wheel of the second wheelset. At this time, the maximum wheel load reduction rate reaches 90% of the allowable limit value of 0.6 for the safety index, which may have an impact on the safe service of the vehicle.

Figure 17b shows that the maximum dynamic wheel load reduction rate of the outer wheel of the second wheelset increases as the curve radius and the superelevation value increase. Specifically, when the curve radius is 14,000 m and the superelevation value is 220 mm, the maximum wheel load reduction rate of the outer wheel of the trailing wheelset is 0.45. This is because the vehicle is in an over-superelevation state, and the centrifugal force when passing through the curve is less than the centripetal force provided by gravity, which in turn causes the wheel load reduction amount of the outer wheel to increase.

Specifically, under equilibrium superelevation conditions, when the curve radii are 7000 m, 8000 m, 12,000 m, and 14,000 m, the maximum dynamic wheel load reduction rates for the inner wheel of the two-position wheelset are 0.29, 0.28, 0.28, and 0.28, respectively. For the outer wheel, the corresponding values are 0.25, 0.26, 0.28, and 0.28. It can be observed that when the curve radii are 12,000 m and 14,000 m, the maximum dynamic wheel load reduction rates for both the inner and outer wheels of the second wheelset under equilibrium superelevation are relatively low and consistent, which contributes to the safety and stability of the vehicle under curve braking conditions.

5. Conclusions

(1) Compared to straight-track braking, curve braking intensifies the lateral vibrations of the bogie frame. As the curve radius diminishes, the roll angle of the bogie frame reduces, which results in more pronounced lateral vibrations. Conversely, the vertical vibrations of the bogie frame show minimal changes.

(2) The geometric parameters of the track have a significant impact on the dynamic characteristics of the first and second wheelsets, including the vertical forces on the inner and outer sides of the primary suspension, wheel–rail interaction, and the lateral forces on the wheelsets. During braking on a curved track with equilibrium superelevation, the

vehicle's dynamic response characteristics show minimal differences compared to braking on a straight track.

(3) Under curved braking conditions, the superelevation value has a significant impact on the lateral forces of the first wheelset. The derailment coefficient of the outer wheel of the first wheelset decreases and then increases as the superelevation value increases, with the minimum value occurring at equilibrium superelevation.

(4) Under curved braking conditions, the phenomenon of wheel load reduction is most significant in the case of the second wheelset. The maximum dynamic wheel load reduction rate of the inner and outer wheels of the second wheelset increases with the decrease in curve radius and decreases with the decrease in superelevation.

(5) When the curve radius is 7000 m and the superelevation is 40 mm, the maximum dynamic wheel load reduction rate of the inner wheel of the second wheelset reaches 0.54, which is 90% of the maximum allowable safety index limit of 0.6. This situation poses a risk to vehicle operational safety. Thus, with a curve radius of less than 7000 m and superelevation of less than 40 mm, there are significant safety risks for vehicles braking at 300 km/h through such curves. This issue demands vigilant monitoring during operation.

(6) In the next phase, efforts will be made to further refine the brake system model and to conduct a dynamic analysis under curve braking conditions, considering the elastic components in floating brake pads and the time-varying friction coefficient. The impact of these factors on bogie vibrations, wheel–rail forces, and the dynamic load reduction rate of the wheels will also be investigated.

Author Contributions: Conceptualization, C.Z. and J.M.; methodology, Z.W. and Z.F.; software, P.L. and M.Y.G.; validation, Z.W.; formal analysis, C.Z.; investigation, Z.F.; resources, J.M.; data curation, P.L.; writing—original draft preparation, C.Z. and M.Y.G.; writing—review and editing, Z.W.; visualization, Z.F.; supervision, J.M.; project administration, J.M.; funding acquisition, J.M. All authors have read and agreed to the published version of the manuscript.

Funding: This work is supported by the National Key Research and Development Program of China (2023YFB3710604), the National Natural Science Foundation of China (No. U22A20181, 52205217), the Young Elite Scientists Sponsorship Program by CAST (No. 2022QNRC001), the Fundamental Research Funds for the Central Universities (No. 2682024CG008) and China Railway Science Research Institute Group Co., Ltd. Research Project (2022YJ321).

Data Availability Statement: Data is unavailable due to privacy.

Conflicts of Interest: Author Chunguang Zhao was employed by the company Tieke Zongheng (Tianjin) Technology Development Co., Ltd. The remaining authors declare that the research was conducted in the absence of any commercial or financial relationships that could be construed as a potential conflict of interest.

References

1. Andrés, V.T.; Martínez-Casas, J.; Denia, F.D.; Thompson, D.J.; Bruni, S. Railway rolling noise in curved tracks: Dynamic modelling of the wheelset and influence of the curve. *J. Sound Vib.* **2024**, *595*, 118738. [CrossRef]
2. Yang, Y.B.; Liu, S.J.; Chen, W. Study on affecting factors of axial force of fastening bolts of axle-mounted brake discs for high-speed trains. *Soil Dyn. Earthq. Eng.* **2021**, *145*, 106740. [CrossRef]
3. Li, Z.Q.; Han, C.; Li, C.; Li, Z.L.; Yang, Z.Y. Study on affecting factors of axial force of fastening bolts of axle-mounted brake discs for high-speed trains. *J. China Railway Sci.* **2024**, *46*, 40–48.
4. Zuo, J.Y.; Han, F.; Hu, W. Reproduction simulation of emergency brake fault feature for subway train. *J. Traffic Transp. Eng.* **2015**, *15*, 44–49.
5. Lu, C.; Wang, Q.; Wang, Z.; Mo, J.; Zhu, S.; Jin, W. Stick–slip characteristic analysis of high-speed train brake systems: A disc–block friction system with different friction radii. *Vehicles* **2023**, *5*, 41–54. [CrossRef]
6. Wu, Q.; Wang, B.; Spiryagin, M.; Cole, C. Curving resistance from wheel-rail interface. *Veh. Syst. Dyn.* **2022**, *60*, 1018–1036. [CrossRef]

7. Kaewunruen, S.; Ngamkhanong, C.; Liu, X. Spectro-temporal responses of curved railway tracks with variable radii of arc curves. *Int. J. Struct. Stab. Dyn.* **2019**, *19*, 1950044. [CrossRef]
8. Fischer, S.; Németh, D.; Horváth, H. Investigation of the track gauge in curved sections, considering hungarian railway lines. *Infrastructures* **2023**, *8*, 69. [CrossRef]
9. Zhai, W.M.; Wang, K.Y. Lateral interactions of trains and tracks on small-radius curves: Simulation and experiment. *Veh. Syst. Dyn.* **2006**, *44*, 520–530. [CrossRef]
10. Sugiyama, H.; Shabana, A.A.; Omar, M.A.; Loh, W.Y. Development of nonlinear elastic leaf spring model for multibody vehicle systems. *Comput. Methods Appl. Mech. Eng.* **2006**, *195*, 6925–6941. [CrossRef]
11. Suárez, B.; Rodriguez, P.; Vázquez, M.; Fernández, I. Safety assessment of underground vehicles passing over highly resilient curved tracks in the presence of a broken rail. *Veh. Syst. Dyn.* **2012**, *50*, 59–78. [CrossRef]
12. Weilguny, R.; Leitner, M.; Brunnhofer, P.; Pospischil, F. Investigation of dynamic gauge widening in small radius curves and its impact on lateral wheel-rail contact forces. *Veh. Syst. Dyn.* **2023**, *62*, 2112–2213. [CrossRef]
13. Yuan, B.; Liao, D.; Jiang, W.; Deng, H.; Li, G.; Gu, J. Effect of tool tilt angle on microstructure, mechanical properties and fracture behavior of dissimilar friction stir lap welding joint of SiCp/ZL101 and ZL101. *J. Mater. Res. Technol.* **2023**, *23*, 4642–4662. [CrossRef]
14. Vladescu, S.-C.; Lumby, R.; Gant, A.; Dyer, H.; Reddyhoff, T. Using lubricant composition to control friction-induced-vibration in an elastomer-steel contact representing a hydraulic seal. *Tribol. Int.* **2024**, *202*, 110346. [CrossRef]
15. Abubakar, A.R.; Ouyang, H.J. Wear prediction of friction material and brake squeal using the finite element method. *Wear* **2008**, *264*, 1069–1076. [CrossRef]
16. Meng, F.H.; Liu, Y.; Wu, Y.; Ma, Y.M.; Chen, H. Research on finite element simulation of braking process of high speed train brake disc and influence of surface scratch on stress field. *J. Mech. Eng.* **2018**, *54*, 42–48. [CrossRef]
17. Hu, H.B.; Tang, G.B.; Cheng, Z.T.; Huang, Z.B. Co-Cr3C2 coating incorporating grain refinement and dislocation density gra-dient to enhance wear resistance of 24CrNiMo steel. *Wear* **2025**, *564-565*, 205752. [CrossRef]
18. Stefanelli, A.; Aprea, M.; Carbone, F.; Romagnuolo, F.; Caresia, P.; Suero, R. Integrated thermomechanical analysis of tires and brakes for vehicle dynamics and safety. *Vehicles* **2024**, *6*, 1637–1647. [CrossRef]
19. Romagnuolo, F.; Avolio, S.; Fichera, G.; Ruffini, M.; Stefanelli, R.; Timpone, F. A co-simulation platform with tire and brake thermal model for the analysis and reproduction of blanking. *Vehicles* **2023**, *5*, 1605–1621. [CrossRef]
20. Zhou, S.X.; Tong, X.; Sun, Y.D.; Shao, J. Research on new structure of high-speed train brake disc based on phase change heat storage principle. *J. Mech. Eng.* **2022**, *58*, 202–210.
21. Pradhan, S. A recursive wheel wear and vehicle dynamic performance evolution computational model for rail vehicles with tread brakes. *Vehicles* **2019**, *1*, 88–115. [CrossRef]
22. Xiang, Z.; Mo, J.; Ouyang, H.; Massi, F.; Tang, B.; Zhou, Z. Contact behaviour and vibrational response of a high-speed train brake friction block. *Tribol. Int.* **2020**, *152*, 106540. [CrossRef]
23. Hertel, B.; Pagenkopf, J.; König, J. Challenges in the (re-)connection of peripheral areas to the rail network from a rolling stock perspective: The case of germany. *Vehicles* **2023**, *5*, 1138–1148. [CrossRef]
24. Sinou, J.-J.; Loyer, A.; Chiello, O.; Mogenier, G.; Lorang, X.; Cocheteux, F.; Bellaj, S. A global strategy based on experiments and simulations for squeal prediction on industrial railway brakes. *J. Sound Vib.* **2013**, *332*, 5068–5085. [CrossRef]
25. Xiang, Z.Y.; Chen, W.; Mo, J.L.; Liu, Q.A.; Fan, Z.Y.; Zhou, Z.R. The effects of the friction block shape on the tribological and dynamical behaviours of high-speed train brakes. *Int. J. Mech. Sci.* **2021**, *194*, 106184. [CrossRef]
26. Wang, Q.; Wang, Z.; Mo, J.; Zhu, S.; Gou, Q. Evaluation of the dynamic behaviors of a train braking system considering disc-block interface characteristics. *Mech. Syst. Signal Process.* **2023**, *192*, 110234. [CrossRef]
27. Zhang, L.; Wang, Z.; Wang, Q.; Mo, J.; Feng, J.; Wang, K. The effect of wheel polygonal wear on temperature and vibration characteristics of a high-speed train braking system. *Mech. Syst. Signal Process.* **2023**, *186*, 109864. [CrossRef]
28. Wang, D.W.; Wu, X.; Xiang, Z.Y.; Mo, J. Investigation on thermo-mechanical coupling characteristics of disc brake system of high-speed train. *J. Southwest Jiaotong Univ.* **2021**, *56*, 428–436.
29. Wang, Z.; Yang, L.; Mo, J.; Zhu, S.; Jin, W. A trailer car dynamics model considering brake rigging of a high-speed train and its application. *Railw. Eng. Sci.* **2023**, *31*, 269–280. [CrossRef]
30. Sadeghi, J.; Rabiee, S.; Felekari, P.; Khajehdezfuly, A. Investigation on optimum lengths of railway clothoid transition curves based on passenger ride comfort. *Proc. Inst. Mech. Eng. Part F J. Rail Rapid Transit* **2023**, *237*, 882–892. [CrossRef]
31. Hao, R. Discussion on the Curve Radius of Beijing-Shanghai High-speed Railway. *J. Railw. Sci. Eng.* **1995**, *4*, 1–9.
32. Wang, Q.; Wang, Z.; Mo, J.; Zhang, L. Non-linear behaviors of the disc brake system under the effect of wheel-rail adhesion. *Tribol. Int.* **2022**, *165*, 107263. [CrossRef]

33. Zhai, W.M.; Sun, X. A detailed model for investigating vertical interaction between railway vehicle and track. *Veh. Syst. Dyn.* **1994**, *23*, 603–615. [CrossRef]
34. Wang, Z.; Allen, P.; Mei, G.; Wang, R.; Yin, Z.; Zhang, W.; Yin, H. Influence of wheel-polygonal wear on the dynamic forces within the axle-box bearing of a high-speed train. *Veh. Syst. Dyn.* **2020**, *58*, 1385–1406. [CrossRef]